S1 The missing situation and accuracy of the Mie product

The missing of the Mie product is more severe than the Ray product, with an average missing rate of 54.9%. This is because the inversion conditions of the Mie channel are more stringent, and the observation signals are strong enough only in thin clouds and thick cloud tops. The specific missing situation is shown in Fig. S1. Similar to the Ray product, the missing rate of Mie wind gradually increases with time. The reasons for missing in different periods are the same as the Ray wind. The difference is that switching to FM-A laser significantly improves the missing of Mie wind. Geographically, the missing rate in oceanic regions is lower than that in the continents, especially in the middle and low latitude oceanic regions. This is because the Mie channel mainly receives backscatter signals from aerosols and clouds. The cloudy weather throughout the year in these ocean regions provides good observation conditions for Mie channel. It should be noted that the abnormal missing of multiple orbits is related to the abnormal background wind during the assimilation process, and this phenomenon was prevalent in these orbits in 2020 and 2021. Figure S1 (c) and (d) show the altitude-longitude and altitude-latitude missing rate profiles of Mie wind. Those areas with low missing rates are mostly areas where aerosols and clouds gather. The equatorial regions have lower missing rates than high-latitude regions. The missing rate in the near surface is lower than that in the high altitude, which is opposite to the Ray product. The aerosols near the surface enhance Mie scattering, resulting in a higher signal-to-noise ratio.

The accuracy performance of the Mie wind at heights of 0-2 km above the surface is also evaluated (Fig. S2). The R of the Mie wind is 0.86, slightly weaker than the Ray winds. And the MAE and RMSE are 1.60 m s^{-1} and 2.34 m s^{-1}, respectively. From a vertical perspective, the performance of Mie winds at the altitudes of 0-0.5 km is poor with obvious positive deviations. This bias is also reflected in the high RMSE and MAE in these altitudes.

S2 The XGB-Wind model and generated Global-ABLWind product derived from the Mie wind product

The results in the main text are based on Ray product. Based on another Mie wind product provided by ESA, similar results were also obtained. This proves the effectiveness and stability of the proposed method. The results obtained from Mie wind are shown in Fig. S3- Fig. S11 and Table S1.

The difference of the XGB wind model on Mie wind product is that in the correction of bottom wind speed, slor replaces bld as one of the key variables (Fig. S3). There is a strong negative correlation between the terrain slope and the positive bias of the bottom wind speed in the measurements of Mie channel. This may be because the uplift movement caused by the large slope is more likely to form clouds. The signal of Mie channel mainly comes from high signal-to-noise ratio signals inside the cloud, while signals under the cloud are easily overwhelmed, resulting in measurement bias. The R^2 of slor and Mie wind bias is 0.84.

Overall, the results under Mie wind conditions are similar to those under Ray wind conditions. But at the upper level, the R of wind speed retrieved from Mie wind product is lower than ERA5 (Fig. S7). This is due to the slightly lower correlation between the input top Mie wind speed constraints and the true value of the RS wind, which affects the accuracy of the upper layer wind speeds.

In addition, the global average wind speed profiles are also retrieved from the Mie wind product. At an altitude of 100 m, there is also a slight underestimation similar to the Ray situation (Fig. S9). The average latitudinal bias is -0.68 m s^{-1}. The global wind speed also shows a distribution of high in marine areas and low in land areas. There is a slight difference in the 100 m wind speed of XGB-Wind between the Ray and Mie situations. This is due to the fact that the more stringent inversion conditions of the Mie channel result in fewer effective observations compared to the Ray channel.

Table S1. Optimized hyperparameters of XGB-Wind model on Mie wind product.

Hyperparameter	Mie
n_estimators	1300
max_depth	4
learing_rate	0.028
min_child_weight	2.5
subsample	0.7
colsample_bytree	0.7
gamma	1.2
reg_alpha	3
reg_lambda	0.1
R	0.85
RMSE	2.59

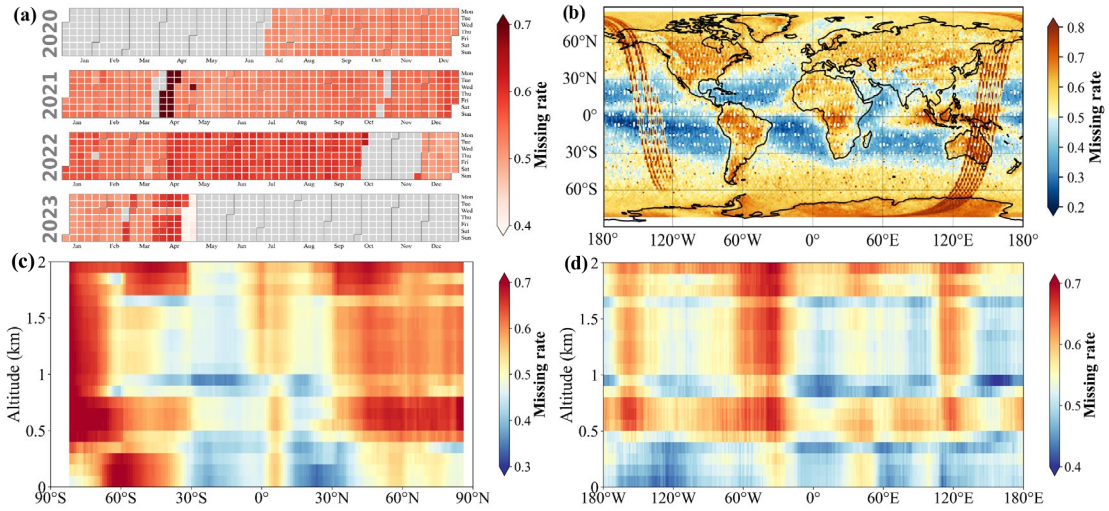

Figure S1. The missing rate of Mie wind below 2 km on a time plane (a), altitude–longitude plane (b), altitude-latitude plane (c), and altitude-longitude plane (d) from July 2020 to April 2023.

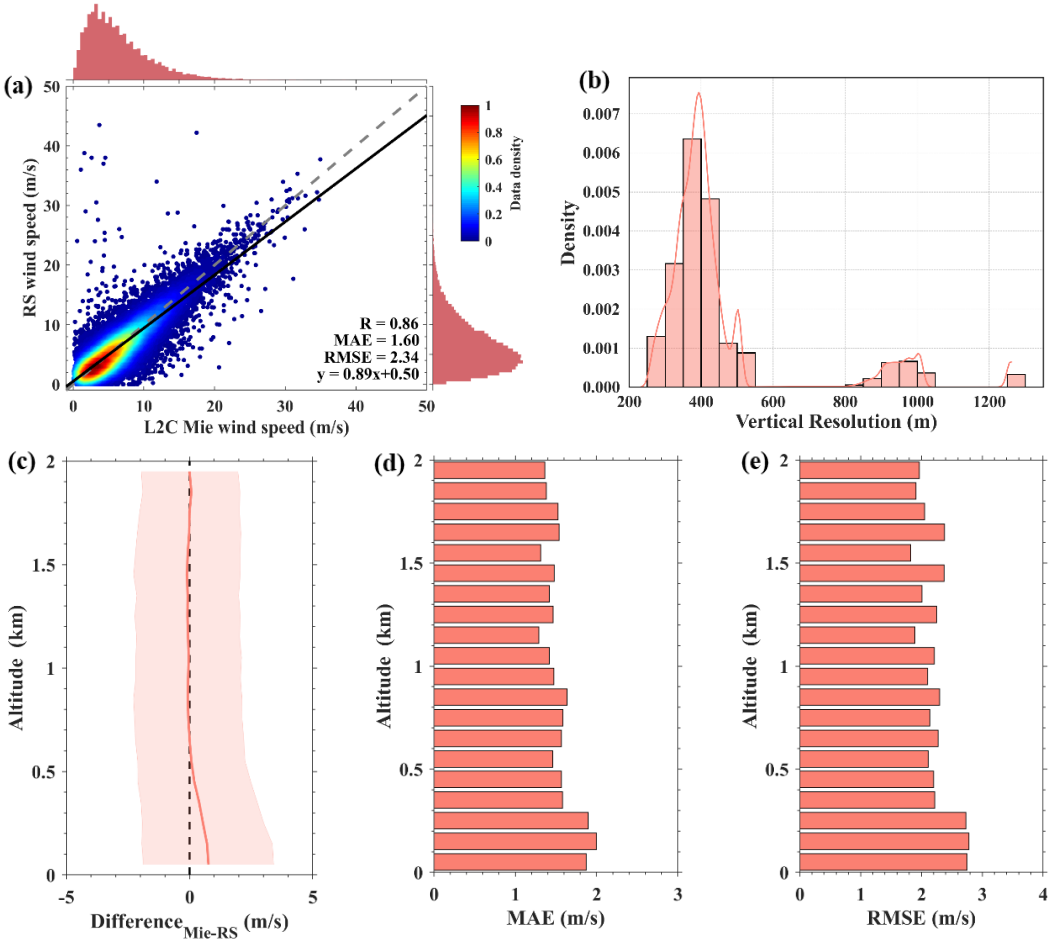

Figure S2. The (a) scatterplot and vertical distributions of (c) bias, (d) MAE, and (e) RMSE between Mie and RS below 2 km. (b) Vertical resolution histogram below 2 km for Mie product and the solid lines are the density curves.

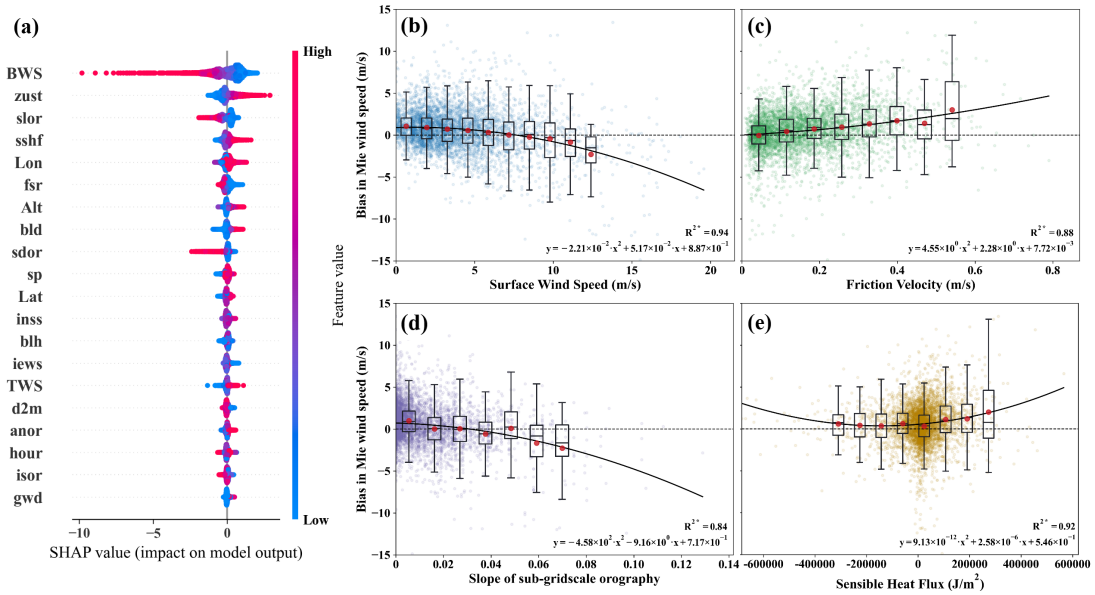

Figure S3. (a) SHAP analysis of the reasons for bottom wind speed bias for Mie wind. BWS: bottom wind speed; zust: friction velocity; slor: slope of sub-gridscale orography; sshf: surface sensible heat flux; Lon: longtitude; fsr: forecast surface roughness; Alt: altitude; bld: boundary layer dissipation; sdor: standard deviation of orography; sp: surface pressure; Lat: latitude; inss: instantaneous northward turbulent surface stress; blh: boundary layer height; iews: instantaneous eastward turbulent surface stress; TWS: top wind speed; d2m: dewpoint temperature; anor: angle of sub-gridscale orography; isor: anisotropy of sub-gridscale orography; gwd: gravity wave dissipation. The Mie wind speed bias below 500 m as a function of (b) surface wind speed, (c) friction velocity, (d) slope of sub-gridscale orography, and (e) sensible heat flux. Red dots and black lines represent the average values of each interval and the fitting curves, respectively.

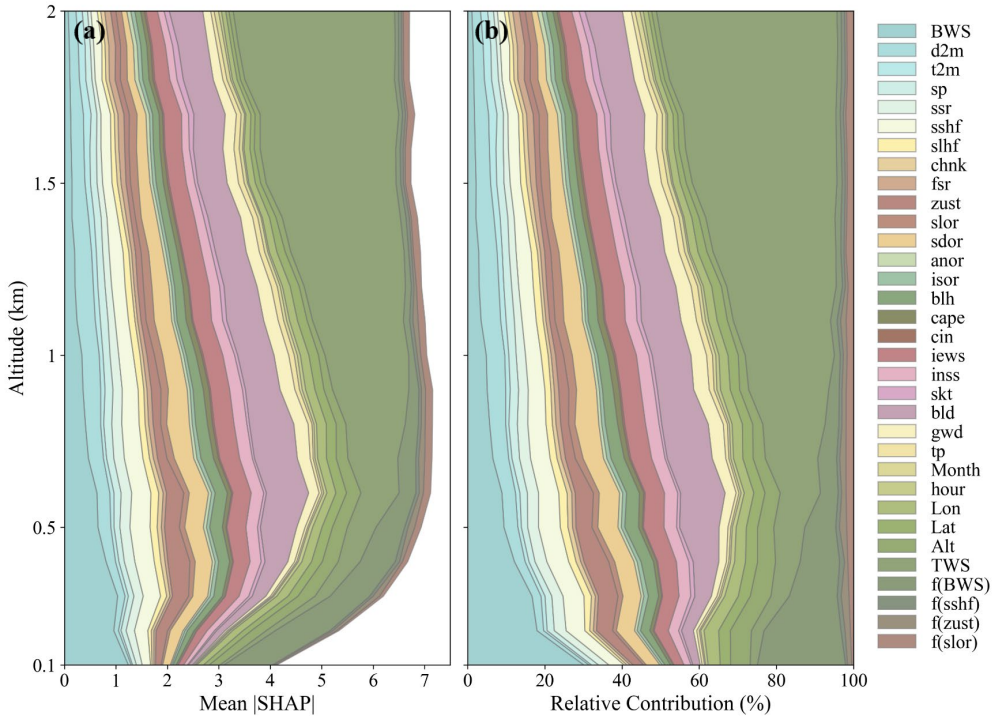

Figure S4. Vertical distribution of (a) mean |SHAP| and (b) relative contribution of |SHAP| of each feature to the XGB-Wind model on the Mie wind product. BWS: bottom wind speed; d2m: dewpoint temperature; t2m: temperature; sp: surface pressure; ssr: surface net solar radiation; sshf: surface sensible heat flux; slhf: surface latent heat flux; chnk: Charnock; frs: forecast surface roughness; zust: friction velocity; slor: slope of sub-gridscale orography; sdor: standard deviation of orography; anor: angle of sub-gridscale orography; isor: anisotropy of sub-gridscale orography; blh: boundary layer height; cape: convective available potential energy; cin: convective inhibition; iews: instantaneous eastward turbulent surface stress; inss: instantaneous northward turbulent surface stress; skt: skin temperature; bld: boundary layer dissipation; gwd: gravity wave dissipation; tp: total precipitation; Lon: longitude; Lat: latitude; Alt: altitude; TWS: top wind speed; f(BWS), f(sshf), f(zust), and f(slor) are the bias corrections calculated by the corresponding variables.

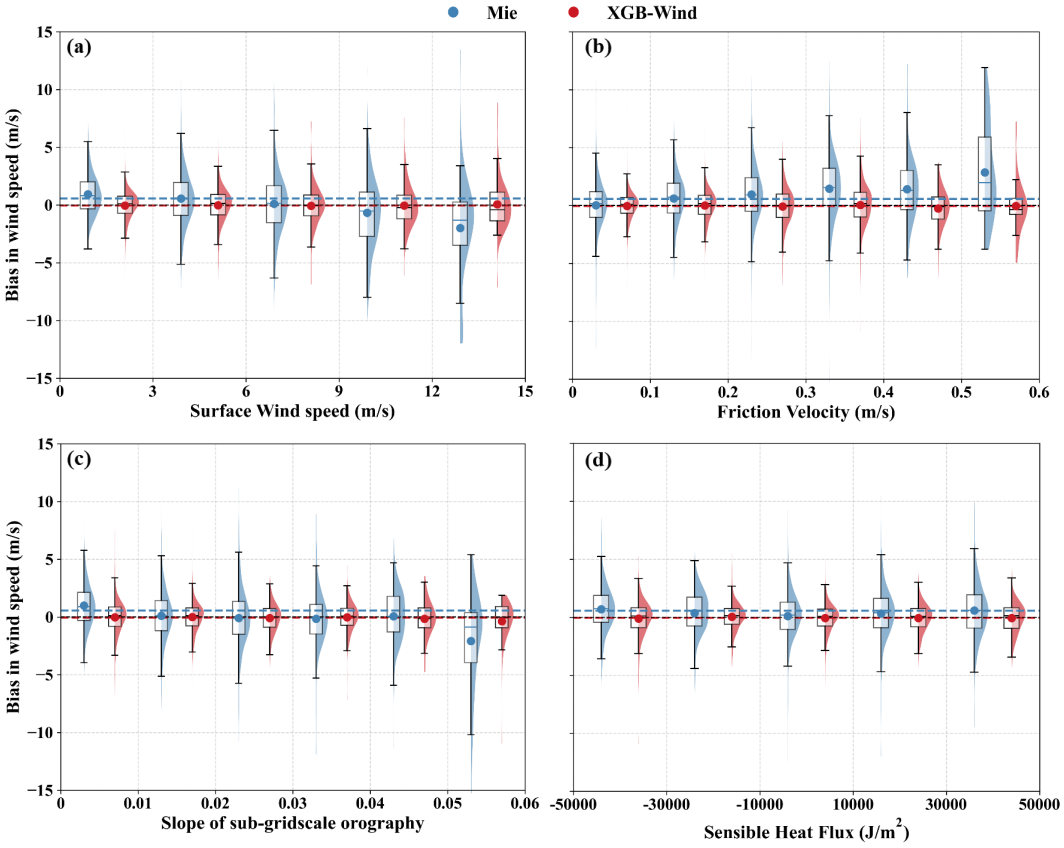

Figure S5. The boxplot of the bias in Mie (blue) and XGB-Wind on Mie wind product (red) below 500 m under varying (a) surface wind speed, (b) friction velocity, (c) slope of sub-gridscale orography, and (d) sensible heat flux. Colored shading denotes the density and dots denote average values.

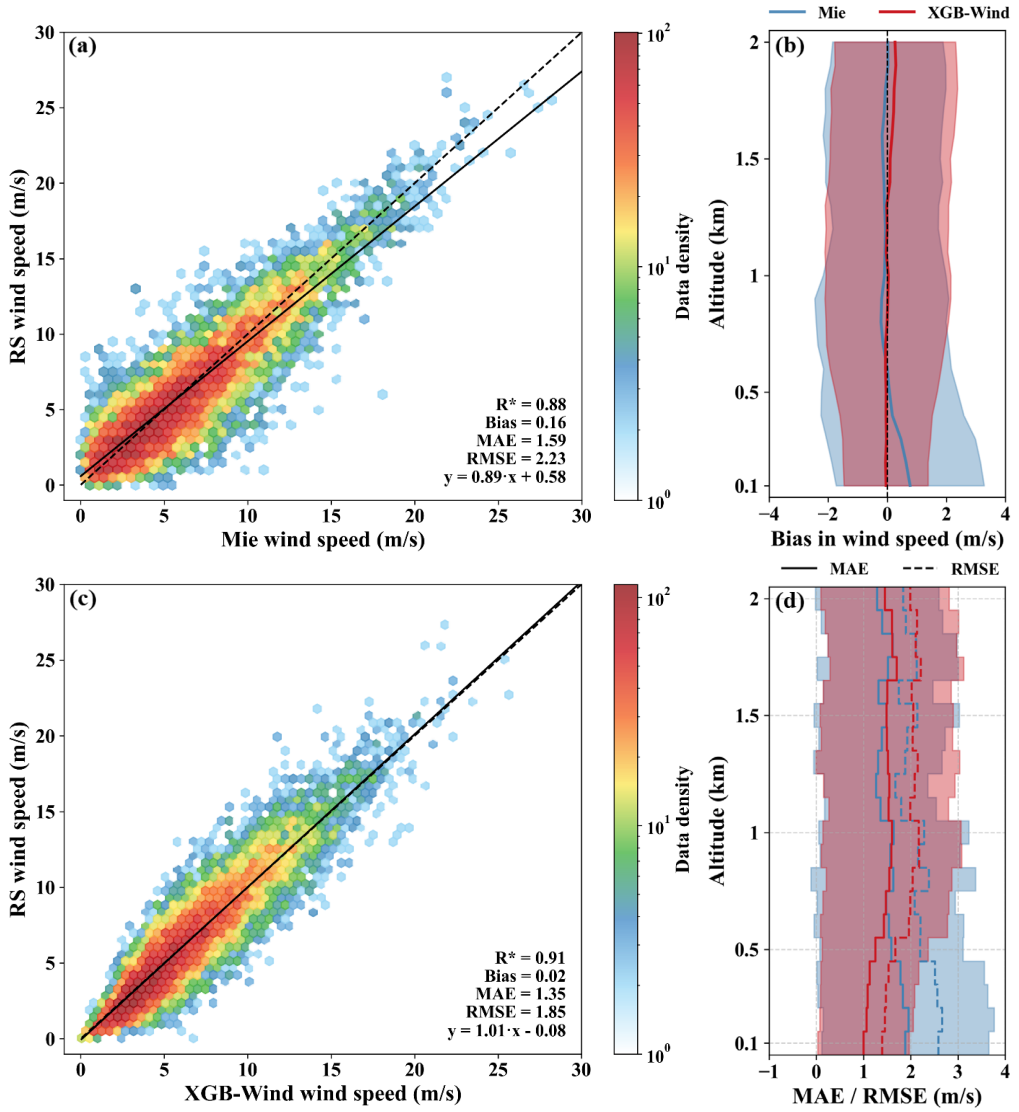

Figure S6. Scatter plots comparing RS-observed wind speeds with estimates from the (a) Mie and (b) XGB-Wind from 0 to 2 km. The dashed line is the 1:1 reference line, the solid lines denote the linear regression fits, and the color bar indicates data density. The asterisk (*) marks R that are statistically significant ($p < 0.05$). Vertical distributions of the (c) bias, (d) MAE and RMSE. Blue and red represent Mie and XGB-Wind, respectively. Colored shading represents the standard deviation. The dashed and solid lines in (d) represent RMSE and MAE, respectively.

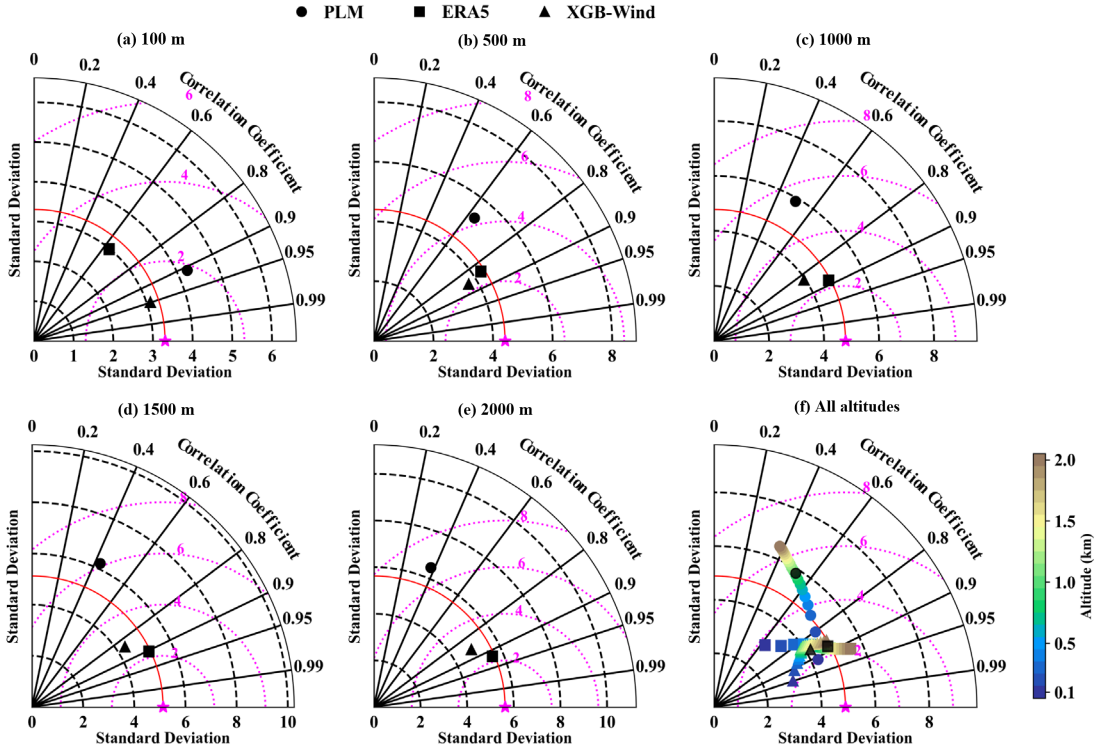

Figure S7. Taylor diagram of the performance of PLM (circles), ERA5 (squares), and XGB-Wind on Mie wind product (triangles) at (a) 100 m, (b) 500 m, (c)1000 m, (d) 1500 m, (e) 2000 m, and (f) all altitudes. In subgraph (f), black represents the results of the entire profile, while color represents the results at different altitudes.

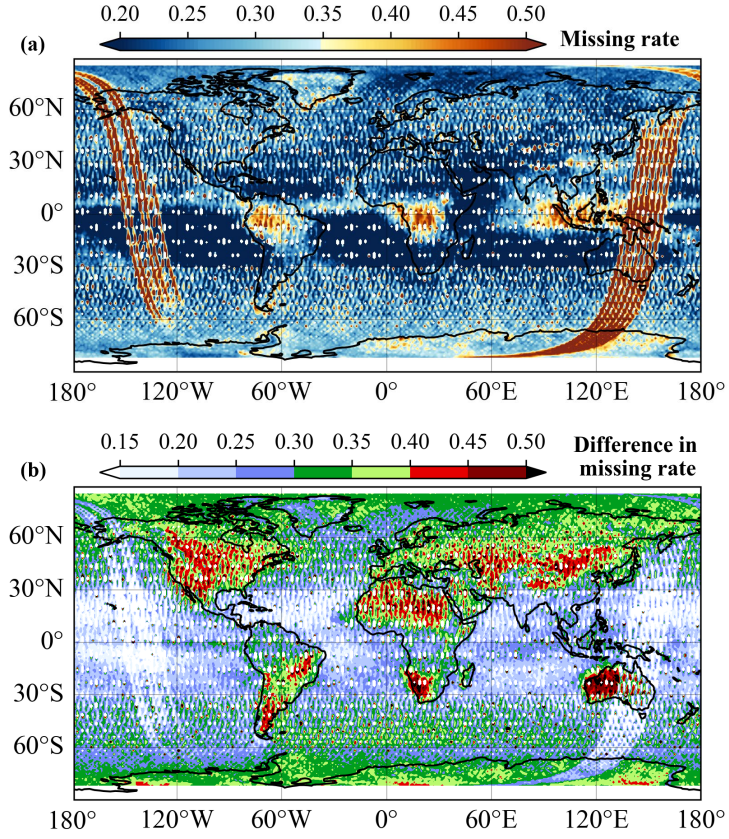

Figure S8. Spatial distribution of (a) the missing rate of the Global-ABLWind product derived from Mie wind product and (b) its improvement in missing rate compared to Mie product.

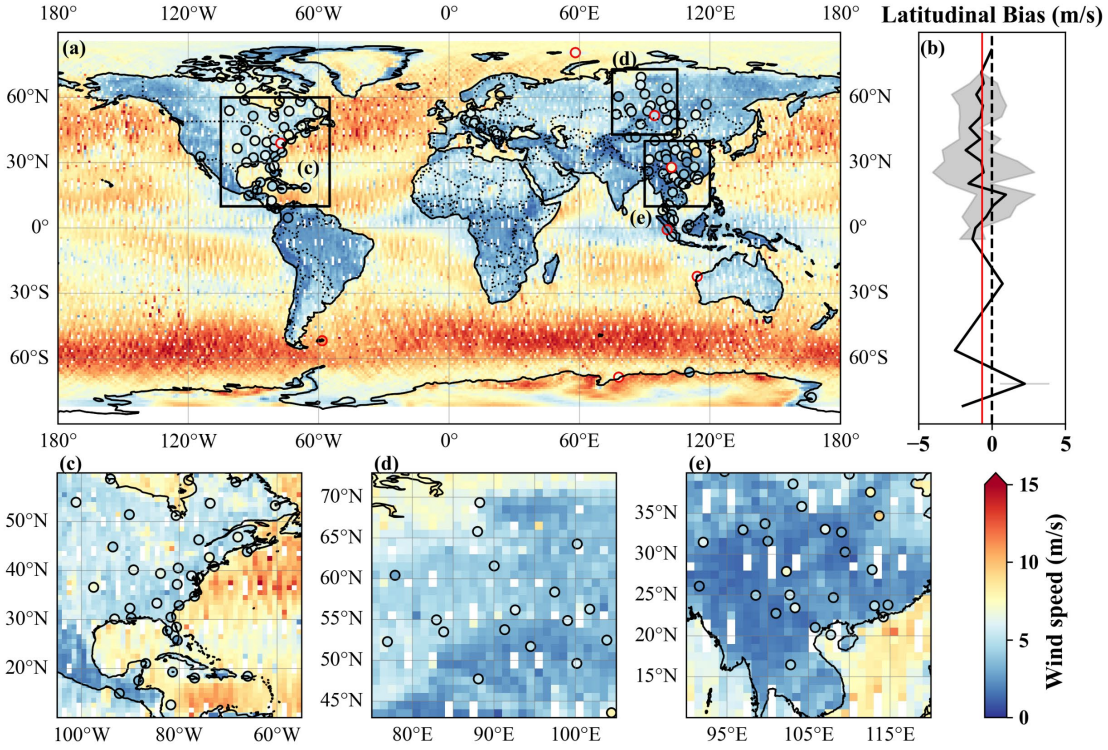

Figure S9. Spatial distributions of the average wind speed at 100 m from the Global-ABLWind product derived from Mie wind product (colored shading) and the RS (colored dots) in 2021 in (a) global, (c) North America, (d) Russia and Central Asia, and (e) China and Southeast Asia. Red-edge dots represent the 8 stations used for subsequent mean profile display. (b) The mean latitudinal bias between Global-ABLWind and RS. The gray shading and red line represent the standard deviation and global mean value, respectively.

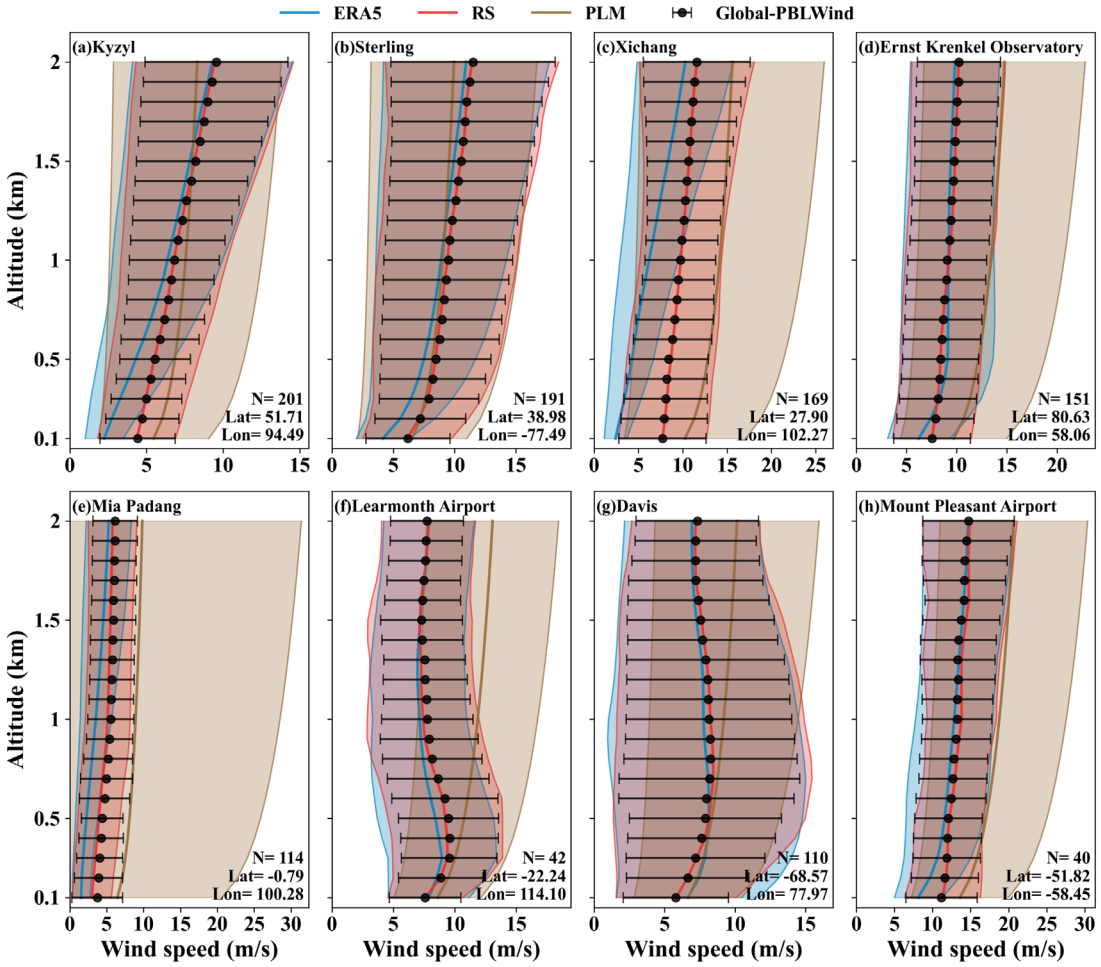

Figure S10. Vertical distributions of average wind speed as derived from multiple methods at (a) Kyzyl, (b) Sterling, (c) Xichang, (d) Ernst Krenkel Observatory, (e) Mia Padang, (f) Learmonth Airport, (g) Davis, and (h) Mount Pleasant Airport. Blue, red, brown, and black represent ERA5, RS, PLM, and Global-ABLWind derived from Mie wind product, respectively. The colored shading or error bars denote the standard deviation.

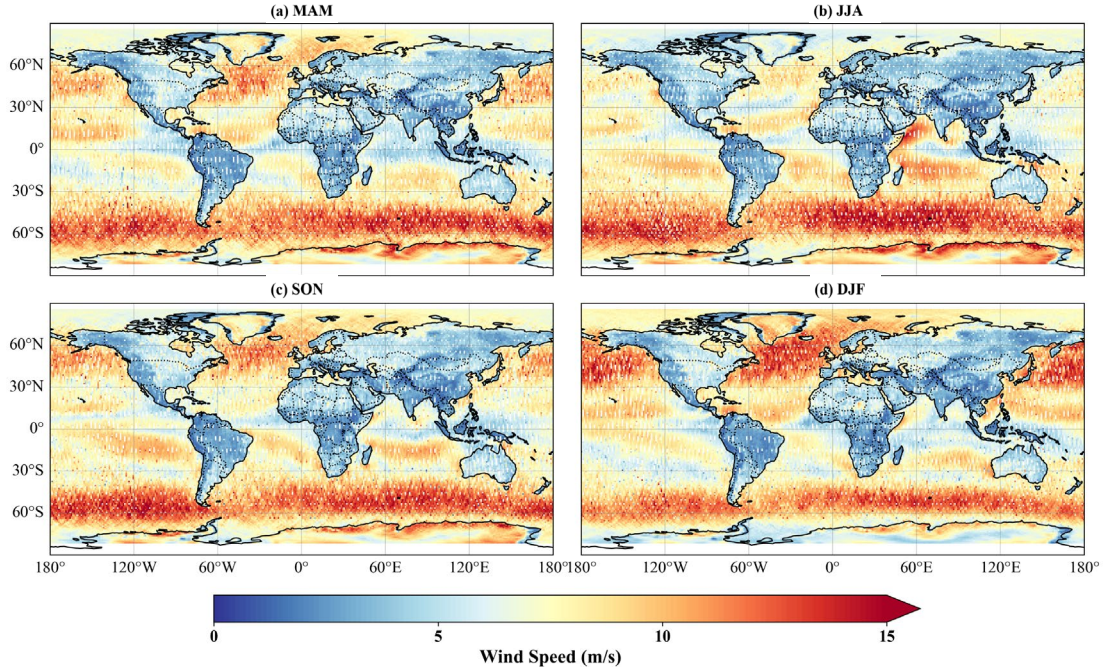

Figure S11. Spatial distributions of the average wind speed at 100 m from the Global-ABLWind product derived from Mie wind product in (a) MAM (March, April, and May), (b) JJA (Jun, July, and August), (c) SON (September, October, and November), and (d) DJF (December, January, and February).